

Comité de suivi individuel :
Electrically driven excitation of Alfvén waves at
low magnetic Reynolds number

Samy Lalloz

July 11, 2022

Introduction

Alfvén waves are Magneto-hydrodynamic (MHD) waves coupling oscillations of magnetic field and velocity field which propagate along the magnetic field. In a short article (1942), Alfvén was the first to theorise the propagation of these waves within in resistive-free medium. Seven years later, Lundquist (1949) confirmed their existence by using a container filled with mercury subjected to a magnetic field of 1.3 Tesla, especially by looking at the velocity of propagation of the waves. In particular, he suggested a condition for the existence of Alfvén waves, where the characteristic propagation time should be lower than the characteristic resistive time. This condition of existence can be easily obtained in medium where the magnetic Reynolds number is high, i.e. when the advection of the magnetic perturbation by the flow dominates the magnetic diffusion. In these media a velocity perturbation perpendicular to a the magnetic field lines will induced a curvature of the latter, which in return, will displace the latter. High magnetic Reynolds numbers can be typically observed in Astrophysics with values ranging up to 10^8 for example in the sun, notably due to the very long characteristic lengths in the latter.

In fact, Alfvén waves are a very intense subject of study in Astrophysics and specially regarding the sun because it could explain the heating process of the latter. In fact, the temperature of the sun atmosphere and especially the solar corona can reach several million Kelvin (Seaton, 1962; Fludra et al., 1999; Aschwanden and Boerner, 2011) while the temperature of the sun surface does not exceed several thousands of Kelvin. Until now, there has been no physical process to quantitatively understand the energy transfer from the surface of the sun to its atmosphere which maintains the high temperature of the solar corona (Zirker, 1993; Taroyan and Erdélyi, 2010). Nevertheless, one of the leading theories to explain this transfer is a heating driven by magneto-hydrodynamics waves which propagate from the lowest atmosphere outward (Zhang and Li, 2004; Roberts, 2000), and transfer heat through a process of damping and MHD turbulence. So, from this theory, Alfvén waves have an important role to play in the energy transfers occurring in the outer part of the sun. However, the study of these waves via the observation made on the sun is a challenge itself. On one hand, it requires high precision measuring instruments in order to have a sufficient resolution to interpret the data. On the other hand, the sun is a complex system where a wide variety of waves can exist. We can for example mention the slow and fast magneto-acoustic waves, like the kink and sausage waves, or the Alfvén waves. Knowing this, it can be difficult to interpret observational data. So, for some observations, there is still no consensus on the nature of the waves observed (Tom; Doorsselaere et al., 2008).

Another way to study the dynamic of Alfvén waves is to force them into a laboratory environment. Thus the objective of the present work is to observe and characterise these waves in a controlled environment that does not allow the development of other waves considered to be parasitic (such as magneto-acoustic waves). The first part of this report is dedicated to the presentation of the theoretical model of Alfvén waves in an experimentally accessible medium, i.e. in a finite geometry with a resistive medium, which provides relevant markers for an experimental study. The second part will present preliminary experimental results and compare them

with theoretical predictions. Finally, the last part will explain the points that still need to be studied and investigated in the framework of this study.

Theoretical model of Alfvén waves in a resistive and bounded medium

Geometry of the axisymmetric model with one injection electrode

The model presented was developed with the aim of relating to the experimental conditions present and accessible with the Flowcube experimental device, initially designed by [Klein and Pothérat \(2010, 2014\)](#), which will be presented in the second part of the report. In particular, two aspects have been taken into account in the model. The first one is the study of the waves in an incompressible resistive MHD framework, relevant for a liquid metal. The second point deals with the wave forcing which depends on time and space.

Let us consider an axisymmetric flow taking place in a cylindrical cavity of radius R and height h subjected to a vertical, static and uniform magnetic field B_0 . In this configuration, the solutions of the flow are assumed to be invariant with respect to the azimuthal angle θ . The domain is bounded by two no-slip conditions at the bottom ($z = 0$) and top ($z = h$) horizontal plates (called Hartmann plates) and filled with a liquid metal (Galinstan) whose characteristics are: electrical conductivity $\sigma_{gal} = 3.4 \times 10^6 \text{ S m}^{-1}$, density $\rho = 6400 \text{ kg m}^{-3}$ and viscosity $\nu = 4 \times 10^{-7} \text{ m}^2 \text{ s}^{-1}$. The wave is forced by injecting an axial current \tilde{j}_z^w through an electrode of radius $\tilde{\sigma}_r$ located at the centre of the bottom Hartmann plate. This current is modelled with a Gaussian distribution along the radial direction:

$$\tilde{j}_z^w = \frac{I_0}{\pi \tilde{\sigma}_r^2} \cdot \exp\left(-\frac{\tilde{r}^2}{\tilde{\sigma}_r^2}\right) \cdot \cos(\tilde{\omega} \tilde{t}), \quad (1)$$

where $\tilde{\omega}$ is the angular frequency of the injected current and I_0 is the amplitude of the current injected by the electrode. From the Maxwell-Ampère equation, it is possible to rewrite the axial current forcing in term of an azimuthal magnetic forcing. Considering the equation (1), it comes:

$$\tilde{b}_\theta^w = \frac{I_0 \mu_0}{2\pi} \cdot \frac{1 - \exp\left(-\frac{\tilde{r}^2}{\tilde{\sigma}_r^2}\right)}{\tilde{r}} \cdot \cos(\tilde{\omega} \tilde{t}), \quad (2)$$

where μ_0 is the vacuum permeability.

The figure 1 shows the modelled domain as well as a qualitative representation of the magnetic and current forcings at the bottom Hartmann plate. Then, we can add the additional boundary conditions necessary to close the problem, which are two non-slip boundary conditions for the velocity and a zero magnetic field at the top plate:

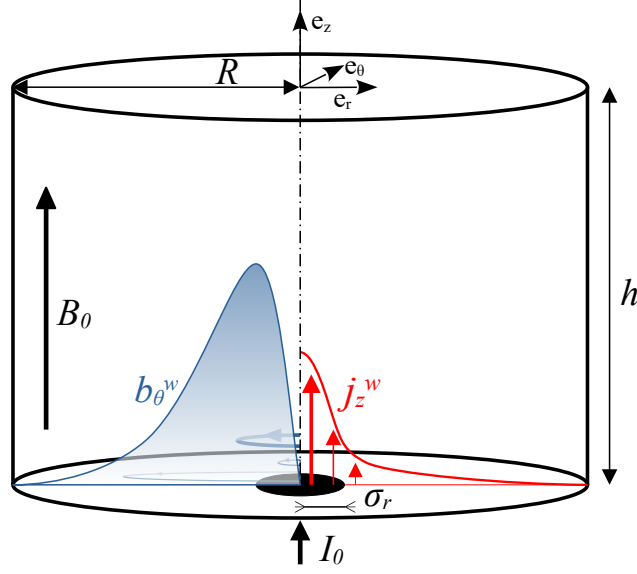


Figure 1: Sketch of the modelled domain with a representation of the bottom boundary condition for the magnetic perturbation. The right side shows the distribution of the axial current injected by the electrode of radius $\tilde{\sigma}_r$ and the left side shows the distribution of the azimuthal magnetic perturbation induced by the axial current.

$$\begin{cases} \tilde{b}_\theta(\tilde{z} = 0, \tilde{r}, \tilde{t}) = \tilde{b}_\theta^w(r) \cdot \cos(\tilde{\omega} \tilde{t}), \\ \tilde{b}_\theta(\tilde{z} = h, \tilde{r}, \tilde{t}) = 0, \\ \tilde{u}_\theta(\tilde{z} = 0, \tilde{r}, \tilde{t}) = 0, \\ \tilde{u}_\theta(\tilde{z} = h, \tilde{r}, \tilde{t}) = 0, \end{cases} \quad (3)$$

Governing equations and method of resolution

As already mentioned in the previous section, the governing equation of Alfvén wave in the medium of concern are the equations of the incompressible resistive MHD. However it should be stated that contrary to the classical study of resistive MHD fluids, i.e. with a low magnetic Reynolds number, the induced magnetic field is not assumed to be zero. Indeed, the Alfvén waves propagation is expressed in particular through the propagation of this induced magnetic field. Thus we can introduce the governing equations for this study, which are the momentum equation:

$$\rho \frac{\partial \tilde{\mathbf{u}}}{\partial \tilde{t}} + (\tilde{\mathbf{u}} \cdot \tilde{\nabla}) \tilde{\mathbf{u}} = -\tilde{\nabla} p + \rho \nu \tilde{\Delta} \tilde{\mathbf{u}} + \mu_0^{-1} (\tilde{\nabla} \times \tilde{\mathbf{b}}) \times \mathbf{B}_0, \quad (4)$$

and the induction equation:

$$\frac{\partial \tilde{\mathbf{b}}}{\partial \tilde{t}} = \tilde{\nabla} \times (\tilde{\mathbf{u}} \times \mathbf{B}_0) + \eta \tilde{\Delta} \tilde{\mathbf{b}}, \quad (5)$$

where $\tilde{\mathbf{b}}$ and $\tilde{\mathbf{u}}$ are respectively the magnetic and the velocity perturbations, p the pressure and η the magnetic diffusivity. $\tilde{\nabla}$ is the Del operator and $\tilde{\Delta}$ the Laplacian

operator. In addition, the solenoïdal nature of the both fields needs to be taken into account:

$$\tilde{\nabla} \cdot \tilde{\mathbf{u}} = 0, \quad (6)$$

$$\tilde{\nabla} \cdot \tilde{\mathbf{b}} = 0, \quad (7)$$

From now on, we will use dimensionless coordinates $r = \tilde{r}/h$ and $z = \tilde{z}/h$, where the height of the vessel is chosen as the length scale, and dimensionless variables $\mathbf{b} = \tilde{\mathbf{b}} \cdot / (\mu_0 I_0) = \tilde{\mathbf{b}}/b_0$, $\mathbf{u} = \tilde{\mathbf{u}} \cdot h B_0 / (\eta b_0) = \tilde{\mathbf{u}}/u_0$ and $t = \tilde{t} \cdot \eta/h^2 = \tilde{t}/\tau$. From the equations (4-7), using the new scaling mentioned, the scaled governing equation for either the magnetic perturbation or the velocity perturbation can be obtained:

$$\left\{ \left(\frac{\partial}{\partial t} - \left(\frac{\partial^2}{\partial z^2} + \Delta_{\perp} \right) \right) \left(\frac{\partial}{\partial t} - Pr_m \left(\frac{\partial^2}{\partial z^2} + \Delta_{\perp} \right) \right) - S^2 \frac{\partial^2}{\partial z^2} \right\} \{\mathbf{b}, \mathbf{u}\} = 0, \quad (8)$$

where two non-dimensional parameters are introduced, respectively the Lundquist number, $S = \frac{v_a h}{\eta}$ where $v_a = \frac{B_0}{\sqrt{\rho \mu_0}}$ is the Alfvén velocity, and the magnetic Prandtl number, $Pr_m = \frac{\nu}{\eta}$. In addition the Laplacian operator has been split into two terms, $\left(\frac{\partial^2}{\partial z^2} \right)$ related to the parallel to the magnetic field B_0 direction and Δ_{\perp} related to the perpendicular directions.

It is worth to note the equation (8) admits a purely azimuthal solution for either \mathbf{u} or \mathbf{b} , which can be solved independently but are nevertheless linked by the induction equation. Thus, we can choose to express the equation (8) in a reference frame adapted to the geometry of the domain, which is axisymmetric, i.e. in cylindrical coordinates. In this configuration, the perpendicular component of the Laplacian operator projected on \mathbf{e}_{θ} is $\Delta_{\perp} = \frac{\partial^2}{\partial r^2} + \frac{1}{r} \frac{\partial}{\partial r} - \frac{1}{r^2}$. The method of solving for the partial differential equation is based on a generalized Fourier series expansion of the solution. This method uses the eigenvector basis for the spacial and time coordinates. In this geometry, the eigenvector basis is not harmonic with respect to the radial coordinate. One can nevertheless define an eigenvector basis $e_{k_{\perp}}^{\perp}$ thanks to the Sturm-Liouville theory so that one gets: $\Delta_{\perp} e_{k_{\perp}}^{\perp} + k_{\perp}^2 e_{k_{\perp}}^{\perp} = 0$, where k_{\perp}^2 is the associated eigenvalue. For the cylindrical geometry, assuming an axisymmetric and non-divergent magnetic and velocity perturbations at $r = 0$, the eigenvector basis is based on the Bessel function of first kind and first order and the eigenvalues are the square of the roots of these functions normalized by the dimensionless radius of the system. In addition, the form of the magnetic and velocity perturbations are harmonic with respect to the axial coordinate and time. Thus, we can define the form of the disturbance as:

$$\mathbf{a}_{\theta} = \sum_{k_{\perp}, \alpha_z} C_{k_{\perp}, \alpha_z} J_1(k_{\perp} \cdot r) \cdot e^{j(\alpha_z z - \omega t)} + \text{c.c.}, \quad (9)$$

where \mathbf{a}_{θ} can be either b_{θ} or u_{θ} and C_{k_{\perp}, α_z} are the coefficient to determine using the boundary conditions. By injecting this form of solution (9) in the equation (8), we obtain the dispersion relation at a given transverse eigenmode $k_{\perp n}$ governing the behaviour of magnetic and velocity perturbations:

$$Pr_m \alpha_z^4 + ([S^2 + 2Pr_m k_{\perp n}^2] - j\omega [1 + Pr_m]) \alpha_z^2 + .. + (k_{\perp n}^4 Pr_m - \omega^2 - j\omega (1 + Pr_m) k_{\perp n}^2) = 0, \quad (10)$$

As the solution of \mathbf{a}_θ can admit several transverse eigenvalues $k_{\perp n}$, more than one dispersion relation can exist. Moreover, one can note the equation (10) provides two sets of two conjugate solutions $(\pm \alpha_z^+ \pm \alpha_z^-)$ for $j\omega$ and its conjugate. Therefore, it exists 8 solutions for α_z per transverse mode, and as many coefficients C_{k_{\perp}, α_z} . Due to the use of the Bessel series for the radial coordinate, the transverse eigenmodes $k_{\perp n}$ are obtained from the roots of the Bessel functions of the first kind and of order 1. In particular we the relation:

$$k_{\perp n} = \lambda_n \frac{h}{R} = \frac{\lambda_n}{R}, \quad (11)$$

where λ_n is the n^{th} root of J_1 .

After solving the dispersion relation (10) and by setting $\alpha_{zn}^\pm = k_n^\pm - i s_n^\pm$, we can rewrite the solutions for u_θ :

$$u_\theta = \sum_{n=1}^{\infty} J_1(k_{\perp n} r) \left\{ e^{s_n^+ z} (U_n^1 \cos(\omega t + k_n^+ z) - U_n^2 \sin(\omega t + k_n^+ z)) + .. e^{-s_n^+ z} (U_n^3 \cos(\omega t - k_n^+ z) - U_n^4 \sin(\omega t - k_n^+ z)) + .. e^{s_n^- z} (U_n^5 \cos(\omega t + k_n^- z) - U_n^6 \sin(\omega t + k_n^- z)) + .. e^{-s_n^- z} (U_n^7 \cos(\omega t - k_n^- z) - U_n^8 \sin(\omega t - k_n^- z)) \right\}, \quad (12)$$

where U_n^i are the coefficients to determine with the boundary conditions. The solution for b_θ can be written in the same way just by replacing U_n^i by B_n^i . The boundary conditions have already been expressed in the previous subsection (3). However these must be re-expressed in the eigenvector base, i.e. in the form of a generalized Fourier series. This means the distribution b_θ^w , which only depends on the radial coordinate, needs to be expressed in a Bessel series with respect to J_1 . It comes:

$$b_{\theta approx}^w(r) = \sum_{n=1}^{\infty} \beta_n J_1(k_{\perp n} r), \quad (13)$$

where $b_{\theta approx}^w$ is the approximation of the magnetic forcing at the bottom plate b_θ by the Bessel series and β_n results from the projection of b_θ^w on the basis of Bessel functions:

$$\beta_n = \frac{2}{(R J_2(k_{\perp n} R))^2} \int_0^R \zeta b_\theta^w(\zeta) J_1\left(k_{\perp n} \frac{\zeta}{R}\right) d\zeta, \quad (14)$$

From the expression of the magnetic forcing into Bessel series, one can obtain the boundary conditions for each given transverse mode $k_{\perp n}$:

$$\begin{cases} b_{\theta n}(z=0, r, t) = \beta_n J_1(k_{\perp n} r) \cdot \cos(\omega t) \\ b_{\theta n}(z=h, r, t) = 0 \\ u_{\theta n}(z=0, r, t) = 0 \\ u_{\theta n}(z=h, r, t) = 0 \end{cases} \quad (15)$$

where $b_{\theta n}$, resp. $u_{\theta n}$, represents the set of terms of the solution b_{θ} , resp. u_{θ} , for a given transverse mode $k_{\perp n}$.

From these boundary conditions, one can write the set of equations which determines the coefficients U_n^i and B_n^i :

$$\sum_{i=1}^4 U_n^{2i-1} = 0, \quad (16a)$$

$$\sum_{i=1}^4 U_n^{2i} = 0, \quad (16b)$$

$$\begin{aligned} & \cos(k_n^+ h) \left[U_n^1 e^{s_n^+ h} + U_n^3 e^{-s_n^+ h} \right] + \sin(k_n^+ h) \left[-U_n^2 e^{s_n^+ h} + U_n^4 e^{-s_n^+ h} \right] + \\ & \cos(k_n^- h) \left[U_n^5 e^{s_n^- h} + U_n^7 e^{-s_n^- h} \right] + \sin(k_n^- h) \left[-U_n^6 e^{s_n^- h} + U_n^8 e^{-s_n^- h} \right] = 0, \end{aligned} \quad (16c)$$

$$\begin{aligned} & \cos(k_n^+ h) \left[-U_n^2 e^{s_n^+ h} - U_n^4 e^{-s_n^+ h} \right] + \sin(k_n^+ h) \left[-U_n^1 e^{s_n^+ h} + U_n^3 e^{-s_n^+ h} \right] + \\ & \cos(k_n^- h) \left[-U_n^6 e^{s_n^- h} - U_n^8 e^{-s_n^- h} \right] + \sin(k_n^- h) \left[-U_n^5 e^{s_n^- h} + U_n^7 e^{-s_n^- h} \right] = 0, \end{aligned} \quad (16d)$$

$$\sum_{i=1}^4 B_n^{2i-1} = \beta_n, \quad (16e)$$

$$\sum_{i=1}^4 B_n^{2i} = 0, \quad (16f)$$

$$\begin{aligned} & \cos(k_n^+ h) \left[B_n^1 e^{s_n^+ h} + B_n^3 e^{-s_n^+ h} \right] + \sin(k_n^+ h) \left[-B_n^2 e^{s_n^+ h} + B_n^4 e^{-s_n^+ h} \right] + \\ & \cos(k_n^- h) \left[B_n^5 e^{s_n^- h} + B_n^7 e^{-s_n^- h} \right] + \sin(k_n^- h) \left[-B_n^6 e^{s_n^- h} + B_n^8 e^{-s_n^- h} \right] = 0 \quad (16g) \\ & \cos(k_n^+ h) \left[-B_n^2 e^{s_n^+ h} - B_n^4 e^{-s_n^+ h} \right] + \sin(k_n^+ h) \left[-B_n^1 e^{s_n^+ h} + B_n^3 e^{-s_n^+ h} \right] + \\ & \cos(k_n^- h) \left[-B_n^6 e^{s_n^- h} - B_n^8 e^{-s_n^- h} \right] + \sin(k_n^- h) \left[-B_n^5 e^{s_n^- h} + B_n^7 e^{-s_n^- h} \right] = 0 \end{aligned} \quad (16h)$$

Remark: The induction equation makes it possible to express the coefficients of the magnetic perturbation in terms of U_n^i , which reduced the number of unknown independent coefficients by two, and thus allows the closure of the former system.

From these solutions it is possible to build parameters useful for the Alfvén wave characterisation. In particular, we can note two important properties of the waves: the propagation time (called transit time) and the damping (or resonance) ratio. The first parameter is obtained by looking at the phase shift of the velocity perturbation from the bottom plate to the top plate. The second parameter can be studied by looking at the ratio of the amplitude of a given signal at the top plate to the one at the bottom plate. This is done by calculating the maximum amplitude of the velocity perturbation for the both two plates just outside the Hartmann layer (In fact the velocity is zero at the very location of the plates because of the non slip conditions).

Extension to a two-electrodes wave forcing

From the expression of the solutions of the magnetic and velocity perturbations for a single electrode forcing, which is axisymmetric, it is possible to determine the solution for more complex forcings. In fact the solution found in the previous section is achieved using the linearised full resistive MHD equations. Thus, the principle of superposition, valid for a linear study, can be applied to find the solution for a more complex magnetic forcing. Here we have implemented the program to model two electrodes of injection in phase opposition. The goal of this implementation is to get closer to the experimental conditions obtained with the Flowcube device, which is composed of a set of injection electrodes. The next section will be dedicated to a brief reminder of the Flowcube device (for a more detailed description of the latter, please refer to the 2nd year deliverable).

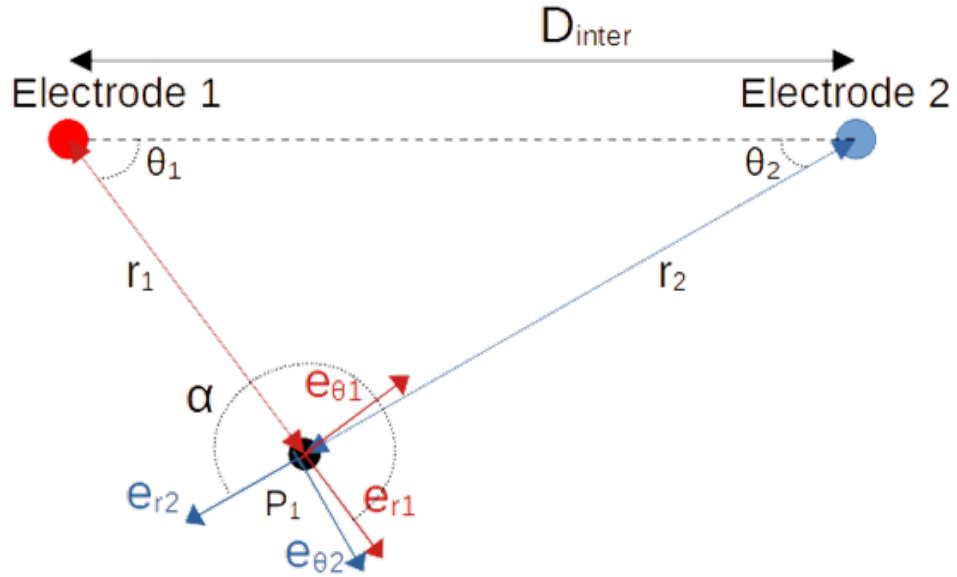


Figure 2: Diagram of the electrodes located at the bottom plate. They are separated a distance D_{inter} apart. The point P_1 represents the location of the wave calculation performed a distance r_1 apart from the electrode 1 and a distance r_2 apart from the electrode 2.

The figure 2 shows the location of the forcing electrodes and the calculation site P_1 . The two electrodes are spaced apart by a length D_{inter} . The complete solution is calculated following this process :

- The coefficients of solution for the electrode 1 are calculated at a distance r_1 apart. This solution S_1 is found in the coordinate basis $\{e_{r1}, e_{\theta1}\}$
- The coefficients of solution for the electrode 2 are calculated at a distance r_2 apart. This solution S_2 is found in the coordinate basis $\{e_{r2}, e_{\theta2}\}$
- The solution S_2 is projected into the coordinate basis of the electrode 1, i.e. $\{e_{r1}, e_{\theta1}\}$. The projection consists of a rotation of an angle α of the solution

S2. This angle α is fully determined by the distances r_1 and D_{inter} and the angle θ_1 .

- The solution S1 and the solution projected S2 are added together
- For convenience, the total solution is projected into a cartesian coordinate system $\{e_x, e_y\}$ whose origin is the centre of electrode 1.

Remark: Unlike the solution with a 1 electrode forcing, which is purely azimuthal for the magnetic and the velocity perturbations, the total solution with a 2 electrodes forcing is not zero for the radial and azimuthal directions (except for some particular locations).

From the total solution, it is possible to have a mapping of our physical parameters of interest, such as the amplitude ratio or the transit time, and thus their spatial dependence in a more realistic configuration.

Progress points of the experimental part

Reminder of the Flowcube device

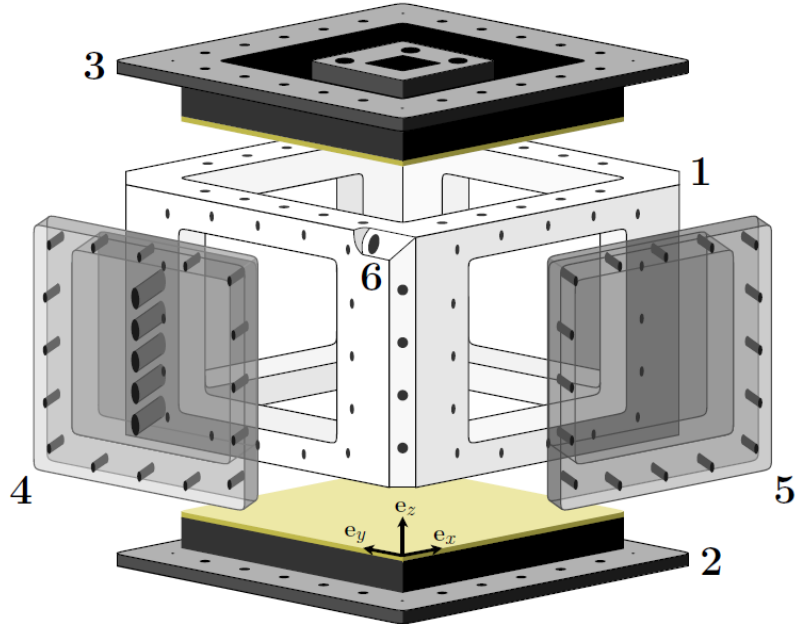


Figure 3: Previous Flowcube device. 1) polyacetal frame; (2) bottom plate (composed of a PCB and a metallic chassis) ; (3) top plate (same composition as the bottom plate) ; (4) ultrasound plate; (5) window; (6) galinstan outlet (inlet is located in the diagonally opposite bottom corner). When the device is subjected to a magnetic field, the latter is along the e_z axis

The design of the device is directly inspired from the the first flowcube device, designed by [Klein and Poth  rat \(2010\)](#). It consists of a cuboid of 15cm side and 10cm height (Fig. 3), filled with a metal alloy liquid at room temperature, Galinstan,

and subjected to a vertical, uniform and static magnetic field B_0 with an amplitude ranging from 3 to 10 Tesla. The bottom and top plates are PCBs composed of a FR4 epoxy layer and a layer of ROGER 4003 (a ceramic acting as a insulator). The forcing of the magneto-mechanics waves is produced by injecting current at the bottom plate of the device thanks to copper made electrodes of 1cm diameter. Then, two methods are used to measure the magnetic and velocity field perturbations induced by the wave propagation. The first one is an array of potential probes located both at the bottom and top plates of the device. This method, called Electric Potential Velocimetry (EPV) can indirectly measure the velocity (in particular orthogonal to the magnetic field components) near the plate of concern by measuring the potential gradient (still the orthogonal to the magnetic field components). This measuring technique has already proven its robustness on several occasions ([Klein and Pothérat, 2014](#)) ([Baker et al., 2017](#)). The second method is the Pulsed Ultrasound Doppler Velocimetry (PUDV), a method based on the principle of echography, which analyses the echoes resulting from the reflection of sound waves upon seeding particles, galinstan oxides in our case, and gives information on the velocity field. The device is composed of few ultrasound probes located on the top and side plates. However, The latter method of measurement is less adapted to investigate Alfvén waves (the accessible frequencies are of the order of a few tens of Hertz).

Experimental protocol

The first experimental campaign has been carried out in February 2022 at the LNCMI (National Laboratory for Intense Magnetic Fields). During two weeks, a set of experiments has been achieved in order to investigate the waves using the Flowcube device. For this set, one injection pattern has been used (Fig. 4). The latter consists of a square of four electrodes located on the bottom plate, spaced 2 cm apart. For this configuration, the slot of potential probes "P3a" has been used. From this pattern, the impact of two parameters has been studied, which are the frequency of the forcing - i.e. the frequency of the injected current - and the strength of the magnetic field. For each magnetic field strength, several forcing frequencies have been studied, in a typically frequency range from 0.1 to 1.1 time the Alfvén frequency, the latter being the inverse of the transit time from the bottom plate to the top plate at the Alfvén velocity. One should note the Alfvén velocity depends on the magnetic field and so does the Alfvén frequency.

Regarding the experimental setup, the current injected and collected by the electrodes is generated using a function generator AFG1000 amplified by a set of two audio amplifiers Behringer EP4000. The injection electrodes are physically connected to the current source via the injection table shown on figure 5. The electric potentials are measured using the potential probes located at the bottom and top plates. These probes are connected to the data acquisition system PXIe-1073, made up of two modules NI PXIe-4303 with a maximum sampling frequency F_s of 51.2 kHz. The sough measurement area is chosen using a home-made mixing board (Fig. 6). From these electric potentials can be obtained the local potential gradient along the x and y axis using a square of four probes.

A typical experimental run consists of the following steps :

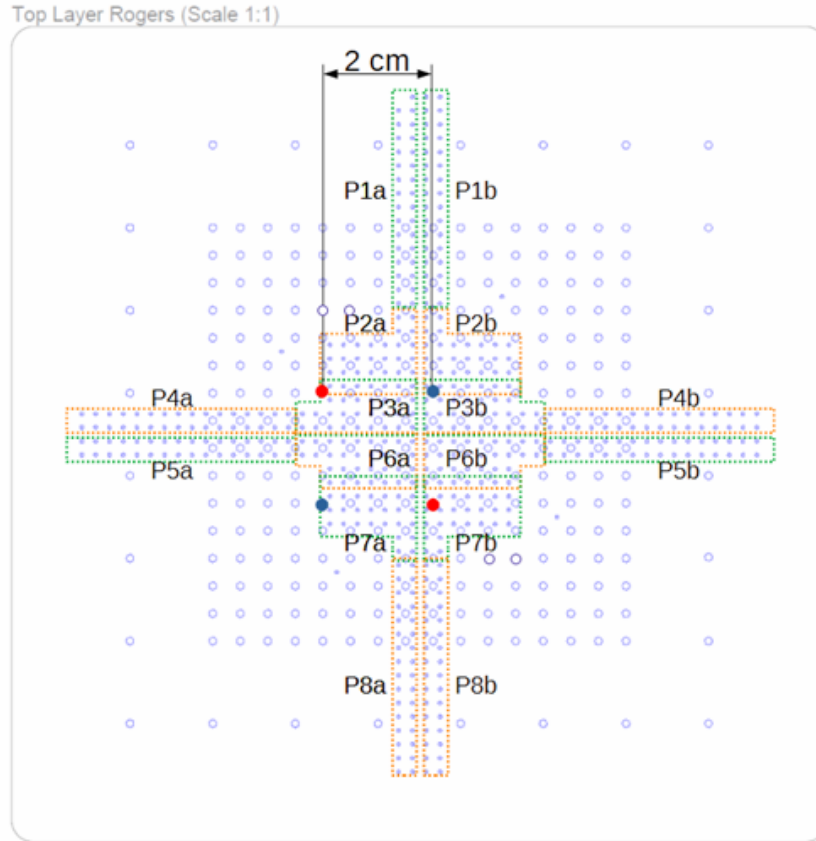


Figure 4: Sketch of the current injection pattern at the bottom plate. The four used injection electrodes are represented by the blue and red rounds. The electrodes with the same colour are at the same phase. Each dotted rectangle represents one slot of potential probes. During this campaign, the slot P3a has been used

1. Apply the magnetic field B_0 at the required strength, wait for the magnetic field to be stabilized
2. Record the electric potential noise for 1:30 min
3. Turn power supply on using the function generator at a given frequency and current intensity.
4. Launch the acquisition of electric potentials for 3 min.
5. Turn off the power supply
6. Repeat the three last steps for each frequency and current intensity to test
7. Record electric potential noise for 1:30 min.

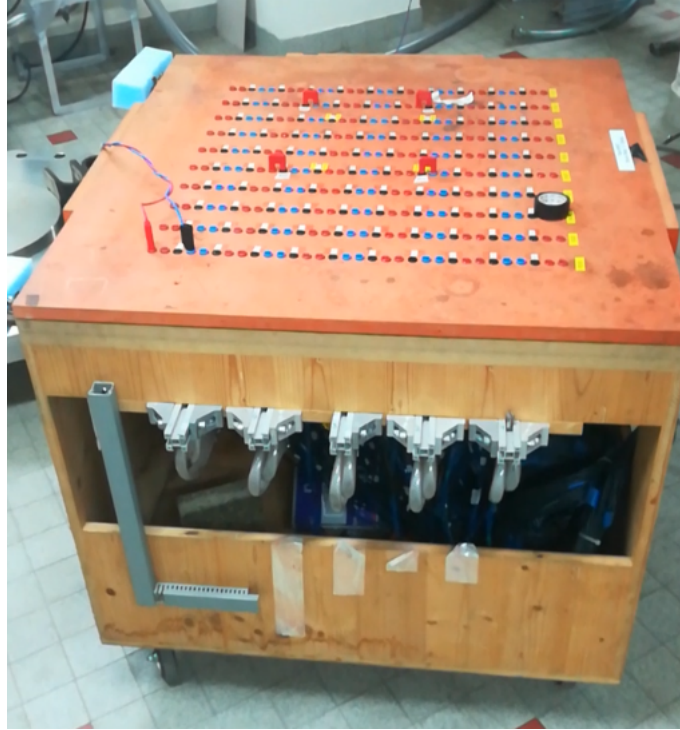


Figure 5: Picture of the table of injection. Each black plug on the table is connected to an electrode at the bottom plate. The red plugs are connected to the same phase of the current source and the blue ones at the opposite phase

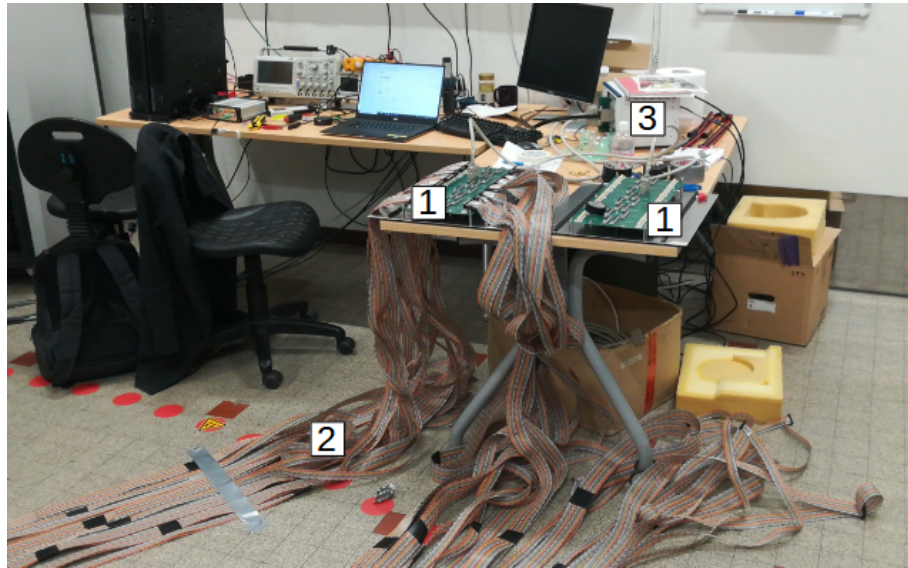


Figure 6: Overview of the acquisition material. (1) mixing board, (2) flat cables connected to the potential probes, (3) acquisition system PXIe-1073

First results from the experimental campaign and comparison with the theoretical model

From the set of experimental trials carried out during the first campaign, a first work of characterisation of the waves has been performed. This one is focus on the

two parameters of interest already mentioned in the modelling section:

- The amplitude ratio of the local potential gradient measured at the horizontal plates.
- The transit time from the bottom plate to the top plate, by looking at the phase shift between the top signals and its corresponding bottom ones.

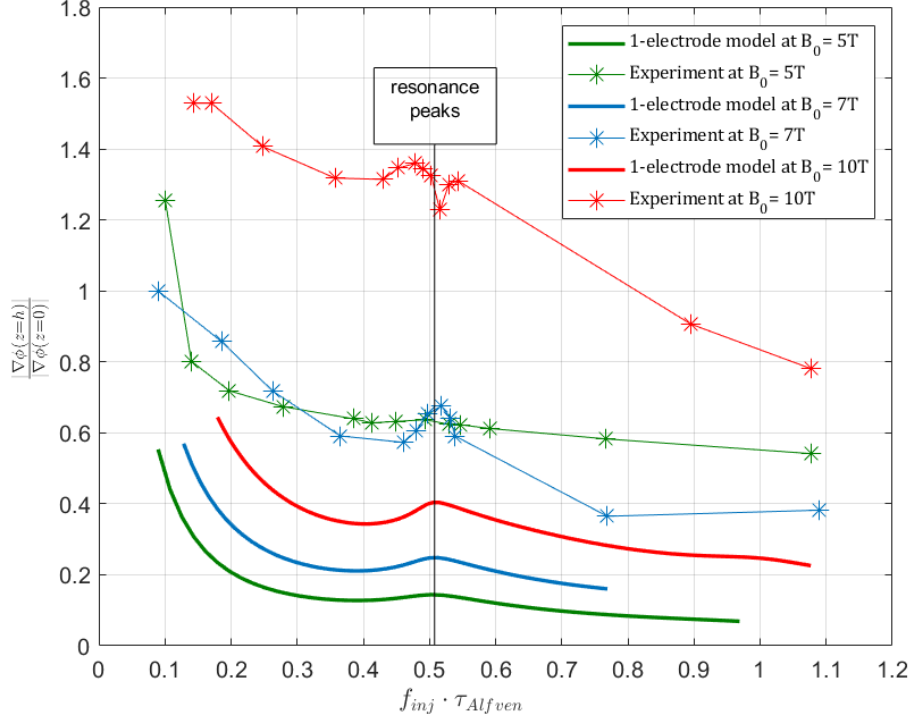


Figure 7: Evolution of the amplitude ratio versus the scaled forcing frequency. The solid lines represent the evolution amplitude ratio predicted by the 1-electrode forcing model for different magnetic field. The lines with star markers represents this evolution from the experimental data

For now, the most promising results are the ones concerning the amplitude ratio parameter. The latter has been studied regarding the frequency of injection for different magnetic fields. The figure 7 shows the evolution of the amplitude ratio of the potential gradient regarding the injection frequency scaled with the Alfvén time. From the model, represented by the solid lines, the main peak of resonance should appear as half the dimensionless frequency. In addition, the value of the peak should rise with the magnetic field. One can note that from the experimental results, the resonance peaks do appear at the frequency predicted by the model. In addition, still from experimental data, the peak of resonance is more pronounced as the magnetic field increases. In particular the local peak is hardly detectable at $B_0 = 5T$, as the model predicts. Other the other hand, some observations are still not fully understood. In fact, the values of the amplitude ratio measured for the three magnetic fields are much higher than those predicted by the model.

For example, at 10 T, the amplitude ratio is higher than one for almost all of the frequency range while in the meantime the model predicts values not higher than 0.8. These observations are, for the moment, not understood.

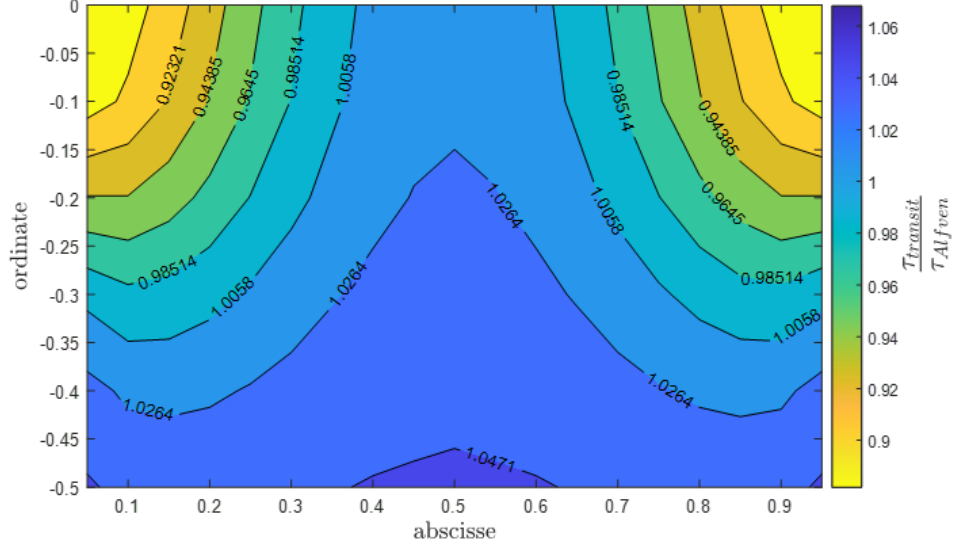


Figure 8: Mapping of the transit time scaled with the Alfvén time, from the 2-electrodes forcing model, regarding the transverse to magnetic field location. The two electrodes of injection are located at (0,0) and at (1,0) and are in phase opposition. The frequency of injection equals to 998 Hz and the strength of the magnetic field equals to 10T

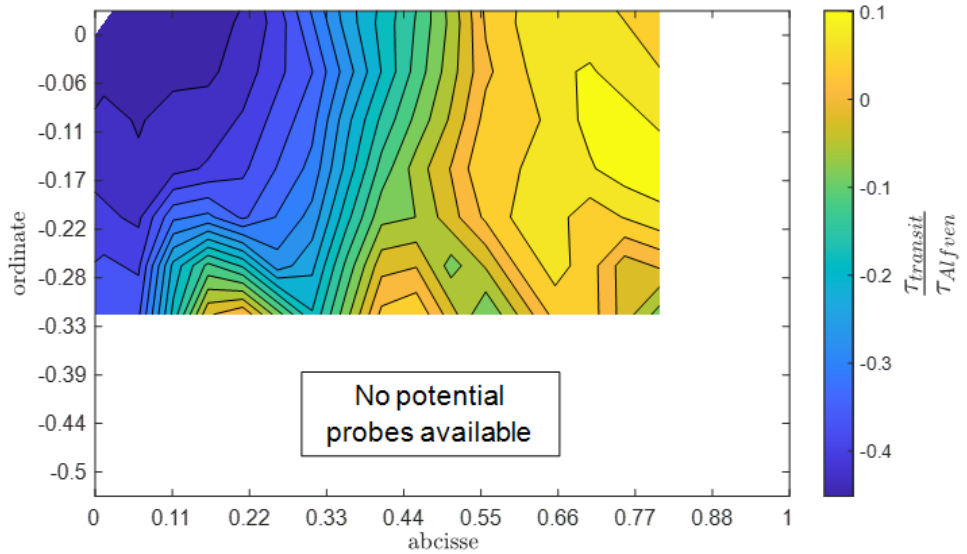


Figure 9: Mapping of the transit time scaled with the Alfvén time, from experiment. The electrodes are located at (0,0) and at (1,0). The frequency of injection equals to 998 Hz and the strength of the magnetic field equals to 10T

Now regarding the transit time, the experimental results are not yet in agreement

with model with two injection electrodes. In fact the figure 8 represents the evolution of the transit time scaled with the Alfvén time regarding the transversal location at an injection frequency of 998 Hz and a magnetic field of 10T. The electrodes are located at points (0,0) and (1,0). From this figure, one can note that the model predicts an increase of the transit time with increasing distance from the nearest electrode, i.e. a decrease of the velocity of propagation of the wave. However the figure 9, which represents the transit time from experiments versus the transverse location at the same conditions, does not reflect the same increase in transit time with increasing distance from the nearest electrode. In fact, the measured transit time includes areas where the transit time corresponds to phase advances, which is not physically possible (areas where the time is positive in the figure 9). This could be manage be applying a modulo operation to transit signal in which case we recover the Alfvén time for the yellow area on the map. However this kind of operation needs to be properly explained to be applied. In addition, the absence of the axis of symmetry at $x = 0.5$ is, for the moment, still not understood. Thus, these experimental data still require further investigation in the future.

Next steps of the research

A summery of the first analysed data has been carried out in the previous section. These results represent a first step in the analysis of Alfvén waves. However, we can already say that there is still more to be done. Thus, the next steps in this study are:

- Continue to work on the data analysis. In particular, try to understand amplitude ratio values obtained higher than expected. In addition, some other trials have been carried out in order to highlight non-linear phenomena of Alfvén waves (by using a double frequency forcing). This points has not been detailed in this deliverable but this aspect is of obvious interest and should also be analysed
- To work on the publication of the results obtained through the writing of an article
- To diffuse the results already obtained via the participation of conferences
- Try to do another set of experiments in December in order to investigation the interaction of the waves with a MHD turbulent flow. The interest would thus be to determine whether or not Alfvén waves can modify the dimensionality of a turbulent MHD flow, in the continuity of the work done by Nataniel Baker [Baker \(2016\)](#).

Bibliography

- H. Alfvén. Existence of electromagnetic-hydrodynamic waves. *Nature*, 150(3805): 405–406, 1942. doi: 10.1038/150405d0.
- S. Lundquist. Experimental investigations of magneto-hydrodynamic waves. *Phys. Rev.*, 76:1805–1809, Dec 1949. doi: 10.1103/PhysRev.76.1805. URL <https://link.aps.org/doi/10.1103/PhysRev.76.1805>.
- MJ Seaton. The temperature of the solar corona. *The Observatory*, 82:111–117, 1962.
- A. Fludra, G. Del Zanna, D. Alexander, and B. J. I. Bromage. Electron density and temperature of the lower solar corona. *Journal of Geophysical Research: Space Physics*, 104:9709–9720, 1999. doi: <https://doi.org/10.1029/1998JA900033>. URL <https://agupubs.onlinelibrary.wiley.com/doi/abs/10.1029/1998JA900033>.
- Markus J. Aschwanden and Paul Boerner. SOLAR CORONA LOOP STUDIES WITH THE ATMOSPHERIC IMAGING ASSEMBLY. i. CROSS-SECTIONAL TEMPERATURE STRUCTURE. *The Astrophysical Journal*, 732(2):81, apr 2011. doi: 10.1088/0004-637x/732/2/81. URL <https://doi.org/10.1088/0004-637x/732/2/81>.
- J. B. Zirker. Coronal heating. 148(1):43–60, 1993. ISSN 1573-093X. doi: 10.1007/BF00675534. URL <https://doi.org/10.1007/BF00675534>.
- Youra Taroyan and R. Erdélyi. *MHD Wave Heating Diagnostics*, pages 287–288. 01 2010. ISBN 978-3-642-02858-8. doi: 10.1007/978-3-642-02859-5_23.
- T. X. Zhang and Bing Li. A kinetic model for resonant heating of ions by alfvén waves in laboratory plasmas. *Physics of Plasmas*, 11(5):2172–2177, 2004. doi: 10.1063/1.1689968.
- B. Roberts. Waves and oscillations in the corona – (invited review). 193(1):139–152, 2000. ISSN 1573-093X. doi: 10.1023/A:1005237109398. URL <https://doi.org/10.1023/A:1005237109398>.
- T. Van Doorselaere, V. M. Nakariakov, and E. Verwichte. Detection of waves in the solar corona: Kink or alfvén? *The Astrophysical Journal*, 676(1):L73–L75, mar 2008. doi: 10.1086/587029. URL <https://doi.org/10.1086/587029>.

- R. Klein and A. Poth  rat. Appearance of three dimensionality in wall-bounded mhd flows. *Phys. Rev. Lett.*, 104:034502, Jan 2010. doi: 10.1103/PhysRevLett.104.034502. URL <https://link.aps.org/doi/10.1103/PhysRevLett.104.034502>.
- Rico Klein and Alban Poth  rat. Why, how and when mhd turbulence at low Rm becomes three-dimensional. *Journal of Fluid Mechanics*, 761:168–205, 2014. doi: 10.1017/jfm.2014.620.
- Nathaniel T. Baker, Alban Potherat, Laurent Davoust, Fran  ois Debray, and Rico Klein. Controlling the dimensionality of low-rm mhd turbulence experimentally. *Experiments in Fluids*, 58(7):1–14, Jun 2017. ISSN 1432-1114. doi: 10.1007/s00348-017-2363-5. URL <https://doi.org/10.1007/s00348-017-2363-5>.
- N. Baker. The dynamics of partly 2d/partly 3d turbulence: an experimental and theoretical study in the low-rm mhd framework, 2016.